Key Engineering Materials
ISSN: 1662-9795, Vol. 926, pp 2040-2049
doi:10.4028/p-3no5jw

Submitted: 2021-12-08
Revised: 2022-01-28
Accepted: 2022-02-03

Estimation of the Effective Magnetic Properties of Two-Phase Steels

Celal Soyarslan[1,a*], Jos Havinga[1,b], Leon Abelmann[2,3,c],
and Ton van den Boogaard[1,d]

[1]Chair of Nonlinear Solid Mechanics, Faculty of Engineering Technology, University of Twente, 7522 NB Enschede, The Netherlands

[2]MESA+ Institute for Nanotechnology, University of Twente, 7522 NB Enschede, The Netherlands

[3]KIST Europe Forschungsgesellschaft mbH, 66123 Saarbrücken, Germany

[a]c.soyarslan@utwente.nl, [b]jos.havinga@utwente.nl, [c]l.abelmann@kist-europe.de,
[d]a.h.vandenboogaard@utwente.nl

Keywords: Electromagnetic Properties, Asymptotic Homogenization, Two-Phase Steels, Metal Forming

Abstract. We investigate the predictive performance of specific analytical and numerical methods to determine the effective magnetic properties of two-phase steels at the macroscale. We utilize various mixture rules reported in the literature for the former, some of which correspond to rigorous bounds, e.g., Voigt (arithmetic) and Reuss (harmonic) averages. For the latter, we employ asymptotic homogenization together with the finite element method (FEM) and periodic boundary conditions (PBC). The voxel-based discretization of the representative volume element is conducted with digital image processing on the existing micrographs of DP600-grade steel. We show that unlike the considered isotropic mixture rules, which use only the phase volume fraction as the statistical microstructural descriptor, finite element method-based first-order asymptotic homogenization allows prediction of both phase content and directional dependence in the magnetic permeability by permitting an accurate consideration of the underlying phase geometry.

Introduction

Big Data and Analytics is considered to be one of the nine pillars of Industry 4.0 [1]. At the factory level, it has already found its way to being widely applied, for example, to logistics problems. On the other side, there is a potential of high benefit when applied at the current production system level. The connection between the production system and computational systems that can be used for analytics and decision making is based on the availability of informative data [2]. In the case of metal forming, this is explicitly challenging, as it is often unfeasible to measure the actual properties of interest during production. Therefore, the development of such systems relies on the acquisition of secondary data that can be connected to the properties of interest by the use of process models [3].

In recent years, several studies have shown the potential of electromagnetic measurements for estimating material formability, which is of significant interest in metal forming [4, 5]. Such non-destructive sensors can potentially be used for in-line control [6]. A disadvantage of the current systems is that these require extensive experimental characterization of the materials for calibration of the sensors.

Instead of data-driven sensor calibration, physics-based models can potentially be used to interpret electromagnetic measurements. The material's microstructure defines its effective physical properties, such as thermo-mechanical or electromagnetic. Given this close connection, electromagnetic sensor data from production lines can be used to infer certain statistical moments of the material microstructure [7, 8, 9, 10, 11, 12] and thus its formability, see Fig. 1. This requires upscaling the microscale properties to macroscale, both in the mechanical and electromagnetic domains. Whereas the connection between microstructure and mechanical properties is being extensively studied in the metal forming and material science community, limited attention has been given to the relation between microstructure and electromagnetic properties in the context of metal forming.

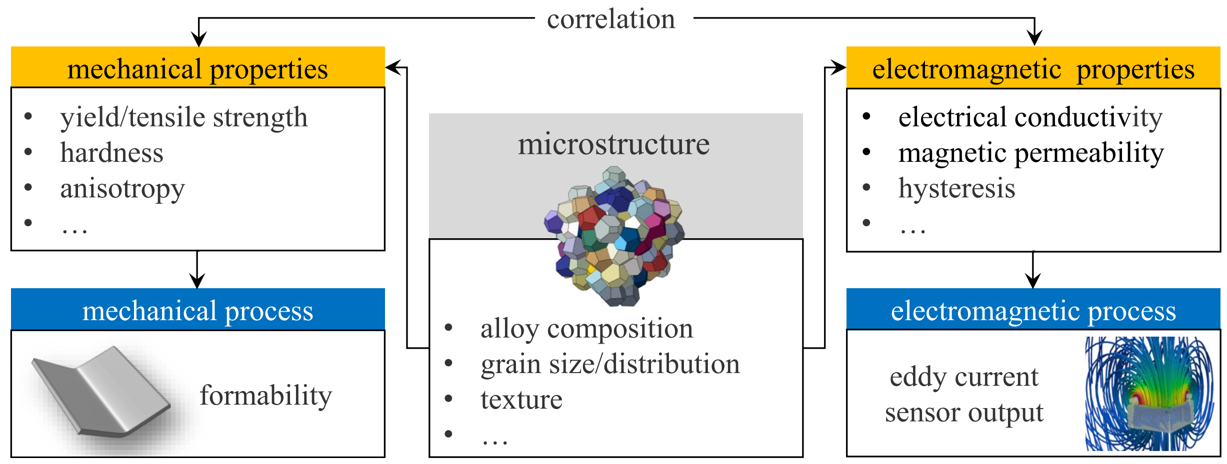

Fig. 1: The microstructure of a material determines its mechanical as well as electromagnetic properties. These properties, which are therefore correlated, control the material's performance in mechanical and electromagnetic processes. This connection allows inference of material's formability through eddy current sensor data acquisition in the production lines. Adapted from [13].

Analytical methods developed to connect the micromagnetic properties to macroscale constitute various effective medium approximations such as the Maxwell Garnett, the Bruggemann, or the power-law rules of mixtures. The (arithmetic) Voigt and the (harmonic) Reuss averages constitute analytical bounds in this respect.

Computational methods which use field averages on material volumes are modeled either as embeddings into free-space with uniform external magnetic fields or as isolated closed-magnetic-circuits [14] subjected to various boundary conditions. In embedded models, due to demagnetizing fields, resultant predictions underestimate the actual magnetic permeability [11]. For the isolated microstructures, besides the boundary conditions proposed in [11], those satisfying Hill-Mandel conditions are discussed in, e.g., [15, 16, 17, 18].

In this work, we use both analytical and numerical methods in prediction of the effective (macroscopic) magnetic properties. Our computational approach relies on first-order asymptotic homogenization, finite element method, and periodic boundary conditions. In the following, we give a detailed account of the unitized analytical estimates and the numerical framework. This is followed by applying the method to some DP600 (two-phase, ferritic/martensitic) steel microstructures for which effective magnetic properties were reported in the literature.

Theory

We consider continua with microstructure comprising two constituent material domains with corresponding volume fractions ϕ_1 and ϕ_2 and magnetic permeabilities μ_1 and μ_2 with the assumption of magnetic isotropy. In the following, we summarize specific analytical and utilize numerical methods to predict the effective electromagnetic properties of such composites.

Analytical Estimates for Effective Permeability of Two-Phase Composites. Considering two-phase composites, the simplest estimates for effective magnetic permeability $\mu^\star$ are those of Voigt and Reuss, which are denoted by $\mu^\star_\mathrm{V}$ and $\mu^\star_\mathrm{R}$, respectively, in the context of isotropic and linear macro-magnetostatics which read

$$\mu^\star_\mathrm{V} = \phi_1\mu_1 + \phi_2\mu_2 \,, \tag{1}$$

$$\mu^\star_\mathrm{R} = [\phi_1{\mu_1}^{-1} + \phi_2{\mu_2}^{-1}]^{-1} \,. \tag{2}$$

The emerging effective magnetic permeability $\mu^\star$ of 3D isotropic composites lies between these estimates with $\mu^\star_\mathrm{R} \le \mu^\star \le \mu^\star_\mathrm{V}$. In addition to the already mentioned Voigt and Reuss estimates, the following analytical solutions exist in the literature for the magnetic permeability of two-phase composites. The Maxwell Garnett mixing rule [19], which is valid for nonvanishing denominator, i.e., $\mu_1 + 2\mu_2 - \phi_1[\mu_1 - \mu_2] \neq 0$, reads

$$\mu^\star_{\text{MG}} = \mu_2 + 3\phi_1\mu_2 \frac{\mu_1 - \mu_2}{\mu_1 + 2\mu_2 - \phi_1[\mu_1 - \mu_2]} \,. \tag{3}$$

On the other hand, the Bruggemann mixing rule [20] results in

$$\phi_1 \frac{\mu_1 - \mu^\star_{\text{B}}}{\mu_1 + 2\mu^\star_{\text{B}}} + \phi_2 \frac{\mu_2 - \mu^\star_{\text{B}}}{\mu_2 + 2\mu^\star_{\text{B}}} = 0 \,. \tag{4}$$

Finally, the power-law (exponential) model gives

$$[\mu^\star_{\text{P}}]^\beta = \phi_1\mu_1^\beta + \phi_2\mu_2^\beta \,. \tag{5}$$

The Reuss and the Voigt forms given in Eqs. (1) and (2) constitute specializations of this rule for $\beta = 1$ and $\beta = -1$, respectively. All above forms satisfy the limiting processes: $\mu^\star = \mu^\star_{\text{V}} = \mu^\star_{\text{R}} = \mu^\star_{\text{MG}} = \mu^\star_{\text{B}} = \mu^\star_{\text{P}} \to \mu_1$ for $\phi_2 \to 0$ and $\mu^\star = \mu^\star_{\text{V}} = \mu^\star_{\text{R}} = \mu^\star_{\text{MG}} = \mu^\star_{\text{B}} = \mu^\star_{\text{P}} \to \mu_2$ for $\phi_1 \to 0$.

Asymptotic Homogenization in Magnetostatics. In development of the asymptotic homogenization method we follow in the footsteps of [21, 22, 23, 24]. A similar application of the theory in electromagnetics for periodic honeycombs can be found in [25]. For convenience, we assume that all forms presented in this section are nondimensional.

Maxwell's equations govern classical electromagnetic field theory [26]. Let, $\boldsymbol{H}$, $\boldsymbol{B}$ respectively denote magnetic field density and magnetic flux density, which are time- and position-dependent electromagnetic vector fields. We consider magnetostatic conditions such that the vector fields do not depend on time, and, thus, their time rate of change vanishes. We also ignore any free current density.

The material system is assumed to be composed of two periodically distributed linearly magnetic phases. This periodicity allows identification of a repeating material domain $\mathcal{V}$, which is henceforth referred to as the unit reference cell. In order to capture both slow and rapid spatial variations of fields and letting the superscript M denote macroscale, we introduce macroscale position ${}^{\text{M}}\boldsymbol{x} \in \mathcal{B}$, with $\mathcal{B}$ denoting the macrocontinuum domain, and microscale position $\boldsymbol{x}$, respectively, which are linked with $\boldsymbol{x} = {}^{\text{M}}\boldsymbol{x}/\epsilon$ where $0 < \epsilon \ll 1$. The considered multiscale fields in this work are $\boldsymbol{H}^\epsilon$-field with $\boldsymbol{H}^\epsilon({}^{\text{M}}\boldsymbol{x}) := \boldsymbol{H}({}^{\text{M}}\boldsymbol{x}, \boldsymbol{x})$ and $\boldsymbol{B}^\epsilon$-field with $\boldsymbol{B}^\epsilon({}^{\text{M}}\boldsymbol{x}) := \boldsymbol{B}({}^{\text{M}}\boldsymbol{x}, \boldsymbol{x})$. Absence of free currents implies that $\boldsymbol{H}^\epsilon$ is conservative and it can be represented as a gradient of the magnetic scalar potential are the magnetic scalar potential $\varrho^\epsilon({}^{\text{M}}\boldsymbol{x}) := \varrho({}^{\text{M}}\boldsymbol{x}, \boldsymbol{x})$ with

$$\boldsymbol{H}^\epsilon = -\boldsymbol{\nabla}_{{}^{\text{M}}\boldsymbol{x}}\varrho^\epsilon \quad \text{in } \mathcal{B}^\epsilon \,. \tag{6}$$

where $\mathcal{B}^\epsilon$ denotes the composite domain. By assuming linear magnetostatics with a $\mathcal{V}-$periodic permeability tensor $\boldsymbol{\mu}$ we have $\boldsymbol{B}^\epsilon = \boldsymbol{\mu}^\epsilon \cdot \boldsymbol{H}^\epsilon$ in $\mathcal{B}^\epsilon$. For convenience, we assume $\boldsymbol{\mu}^\epsilon = \boldsymbol{\mu}(\boldsymbol{x})$ with assumption of isotropy at microscale $\boldsymbol{\mu}_i = \mu_i \boldsymbol{1}$ where μ_i denote magnetic permeability associated with magnetically isotropic phase i, respectively. $\boldsymbol{1}$ denotes the second-order identity tensor. The governing differential equation to be solved is dictated by Gauss's law for magnetism at the composite domain $\mathcal{B}^\epsilon$ with

$$\text{div}_{{}^{\text{M}}\boldsymbol{x}}\boldsymbol{B}^\epsilon = 0 \quad \text{in } \mathcal{B}^\epsilon \,. \tag{7}$$

Applying a two-scale asymptotic expansion of the problem-solution $\varrho^\epsilon({}^{\text{M}}\boldsymbol{x})$ results in the following representation

$$\varrho^\epsilon({}^{\text{M}}\boldsymbol{x}) = \varrho^{(0)}({}^{\text{M}}\boldsymbol{x}, \boldsymbol{x}) + \epsilon\varrho^{(1)}({}^{\text{M}}\boldsymbol{x}, \boldsymbol{x}) + \epsilon^2\varrho^{(2)}({}^{\text{M}}\boldsymbol{x}, \boldsymbol{x}) + \mathcal{O}(\epsilon^3) \,. \tag{8}$$

Here, $\varrho^{(i)}$ are $\mathcal{V}-$periodic functions in $\boldsymbol{x}$. In view of Eq. (8), one derives the following expansions for $\boldsymbol{H}^{\epsilon}$ and $\boldsymbol{B}^{\epsilon}$,

$$\boldsymbol{H}^{\epsilon}({}^{\mathrm{M}}\boldsymbol{x}) = \frac{1}{\epsilon}\boldsymbol{H}^{(-1)}({}^{\mathrm{M}}\boldsymbol{x},\boldsymbol{x}) + \boldsymbol{H}^{(0)}({}^{\mathrm{M}}\boldsymbol{x},\boldsymbol{x}) + \epsilon\,\boldsymbol{H}^{(1)}({}^{\mathrm{M}}\boldsymbol{x},\boldsymbol{x}) + \epsilon^{2}\,\boldsymbol{H}^{(2)}({}^{\mathrm{M}}\boldsymbol{x},\boldsymbol{x}) + \mathcal{O}(\epsilon^{3})\,, \tag{9}$$

$$\boldsymbol{B}^{\epsilon}({}^{\mathrm{M}}\boldsymbol{x}) = \frac{1}{\epsilon}\boldsymbol{B}^{(-1)}({}^{\mathrm{M}}\boldsymbol{x},\boldsymbol{x}) + \boldsymbol{B}^{(0)}({}^{\mathrm{M}}\boldsymbol{x},\boldsymbol{x}) + \epsilon\,\boldsymbol{B}^{(1)}({}^{\mathrm{M}}\boldsymbol{x},\boldsymbol{x}) + \epsilon^{2}\,\boldsymbol{B}^{(2)}({}^{\mathrm{M}}\boldsymbol{x},\boldsymbol{x}) + \mathcal{O}(\epsilon^{3})\,, \tag{10}$$

with $\boldsymbol{B}^{(k)} = \boldsymbol{\mu}\cdot\boldsymbol{H}^{(k)}$ for $k \geq -1$, and substituting the latter expansion in Gauss's law for magnetism given in Eq. (7) and comparing coefficients of powers in ϵ and applying separation of variables, along with introduction of a $\mathcal{V}-$periodic corrector function $\chi^{m}(\boldsymbol{x})$ for $m = 1, 2, 3$, we reach the following macroscopic magnetic permeability tensor $\boldsymbol{\mu}^{\star}$

$$\mu^{\star}_{im} = \frac{1}{|\mathcal{V}|}\int\limits_{\mathcal{V}} \mu_{ik}\left[\delta_{km} + \frac{\partial\chi^{m}(\boldsymbol{x})}{\partial x_{k}}\right]\mathrm{d}V\,, \tag{11}$$

which sets the stage for the constitutive behavior at macroscale with ${}^{\mathrm{M}}\boldsymbol{B} = \boldsymbol{\mu}^{\star}\cdot{}^{\mathrm{M}}\boldsymbol{H}$. Here ${}^{\mathrm{M}}\boldsymbol{B}$ and ${}^{\mathrm{M}}\boldsymbol{H}$ correspond to macroscopic magnetic fields which are computed with the following volume averaging operations on their microscopic (cell-level) counterparts $\boldsymbol{B}^{(0)}$ and $\boldsymbol{H}^{(0)}$

$${}^{\mathrm{M}}\boldsymbol{B} = \frac{1}{|\mathcal{V}|}\int\limits_{\mathcal{V}}\boldsymbol{B}^{(0)}\mathrm{d}V \quad \text{and} \quad {}^{\mathrm{M}}\boldsymbol{H} = \frac{1}{|\mathcal{V}|}\int\limits_{\mathcal{V}}\boldsymbol{H}^{(0)}\mathrm{d}V\,. \tag{12}$$

Derivation of the components $\mu^{\star}_{im}$ is possible by means of finite element discretization of the unit cell domain. To this end, three separate solutions for the nondimensional magnetic scalar potential indexed with m with $\psi^{m}(\boldsymbol{x}) = -\chi^{m}(\boldsymbol{x}) - \varpi^{m}(\boldsymbol{x})$ with $\varpi^{m}(\boldsymbol{x}) = x_{m}$ are used. This creates unitary macroscopic magnetic fields, which allows rewriting Eq. (11) as

$$\mu^{\star}_{im} = \frac{1}{|\mathcal{V}|}\int\limits_{\mathcal{V}} B^{(0)}_{i}(\psi^{m})\,. \tag{13}$$

In view of Eq. (13), determination of the each column vector of the matrix representation of $\boldsymbol{\mu}^{\star}$ requires computation of the averaged magnetic field ${}^{\mathrm{M}}\boldsymbol{B}$ for three separate load cases for $m = 1, 2, 3$.

Application

The framework mentioned above is implemented into ABAQUS [27]. In this work, we determine effective magnetic permeabilities of some ferritic/martensitic DP600-grade steels, for which the micrographs and corresponding effective and constituent material properties were reported in [28].

In Fig. 2, optical micrographs for DP600-grade steel microstructures that differ in the applied heat treatment are given. In [28], about ten images for each heat treatment are used. However, in the current work, only one image for each heat treatment is considered. Each heat treatment condition changes the carbon content in martensite due to the different ferrite-martensite phase balance, which in turn results in a change of the final martensite permeability, the magnitude of which lie in the interval from $47\mu_0$ to $56\mu_0$ [28]. Here, μ_0 represents the magnetic permeability of free space. Considering its convenience in the application of the analytical mixing rules, we use a single permeability value of $\mu_{\mathrm{Mar}} = 55\mu_0$, see, e.g., [28, p. 112]. Therein, the permeability of the ferritic phase is given as $\mu_{\mathrm{Fe}} = 330\mu_0$.

The binarized images for the optical micrographs of the material given in Fig. 2 are depicted in Fig. 3. Binarization is done using the open-source image analysis platform Fiji (ImageJ) [29] with first converting the images to type 8-bit and then application of auto thresholding with the default method, which is a variation of the IsoData [30] algorithm. The binarized images are converted to finite element

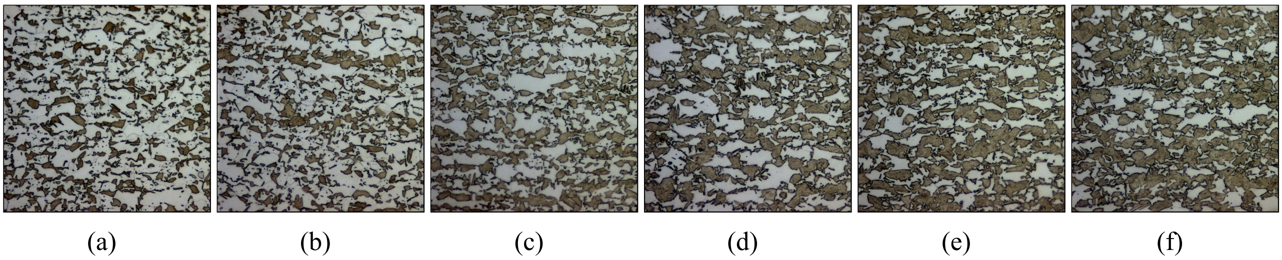

Fig. 2: Optical micrographs for (a) DPL600-650, (b) DPL600-675, (c) DPL600-700, (d) DPL600-725, (e) DPL600-750 and (f) DPL600-800. Here, the darker regions belong to martensite whereas the remaning domain is ferrite. A usable 750×750 sized subregion is clipped out from the original images given in [28]. The direction horizontal to the images, henceforth given by $x-$direction with unit base vector denoted by $\boldsymbol{e}_1$, gives the rolling direction. The transverse direction is $y-$direction with unit base vector denoted by $\boldsymbol{e}_2$.

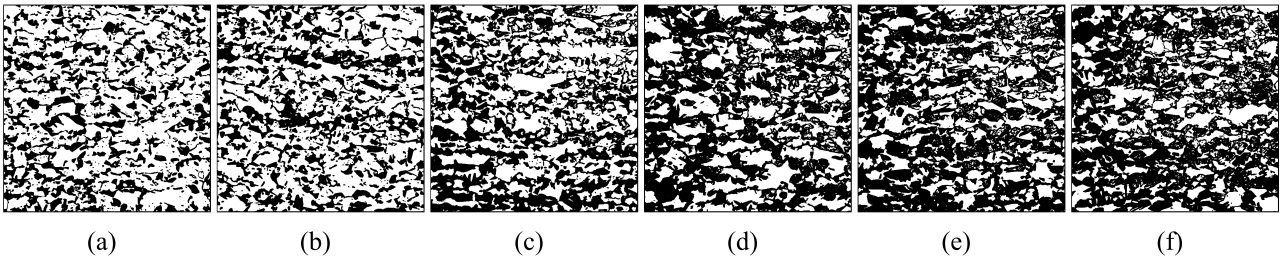

Fig. 3: The binarized microstructural images, corresponding to the optical micrographs of the material given in Fig. 2. Here the white regions denote ferrite phase and the black regions are martensitic where the ferritic phase volume fraction, computed from the area proportions, are computed from (a) to (f) as $\phi_{\text{Fe}} = \{0.64, 0.61, 0.50, 0.43, 0.40, 0.38\}$, respectively.

models using the developed MATLAB scripts. The corresponding finite element discretizations are composed of 562500 4-node linear quadrilateral elements, where the total number of nodes is 564004.

Considering the 2D nature of the problem and in view of Eq. (13), each column vector of the matrix representation of $\boldsymbol{\mu}^\star$ for each microstructure is computed through averaging the resultant magnetic field ${}^{\text{M}}\boldsymbol{B}$ for two separate load cases for $m = 1, 2$ for which the unit cell is subjected to unitary macroscopic magnetic fields with ${}^{\text{M}}\boldsymbol{H} = [1, 0]^\top$ and ${}^{\text{M}}\boldsymbol{H} = [0, 1]^\top$, respectively. The corresponding contour plots for the resultant magnetic scalar potential on the unit cell are given in Fig. 4. In these figures, the results are given for DPL600-650 and DPL600-800. Although the magnetic scalar potential distribution seems linear, it is noisy due to microstructural heterogeneities and material property contrast. This causes fluctuations that are periodic on the boundaries due to the application of periodic boundary conditions. The uniqueness of the fluctuation field is guaranteed by assuming a fixed magnetic scalar at the cell center.

In Fig. 5, the distribution of magnetic flux densities are given for the given unitary macroscopic fields of ${}^{\text{M}}\boldsymbol{H} = [1, 0]^\top$ and ${}^{\text{M}}\boldsymbol{H} = [0, 1]^\top$ for DPL600-650 and DPL600-800. It is observed that the magnetic flux lines are concentrated on the high permeability ferritic phase, which is higher in volume percentage for the first row results. With increasing ferrite content, the possibility of finding percolating ferrite pathways increases. This is apparent in the higher resultant magnetic flux magnitudes observed for DPL600-650 for which $\phi_{\text{Fe}} = 0.64$ as compared to DPL600-800 where $\phi_{\text{Fe}} = 0.38$. The influence of the microstructural anisotropy due to rolling is also apparent in these plots. With the resultant banded nature, increased ferrite phase percolation (long-range connectivity) along the rolling direction effectively hosts magnetic flux lines.

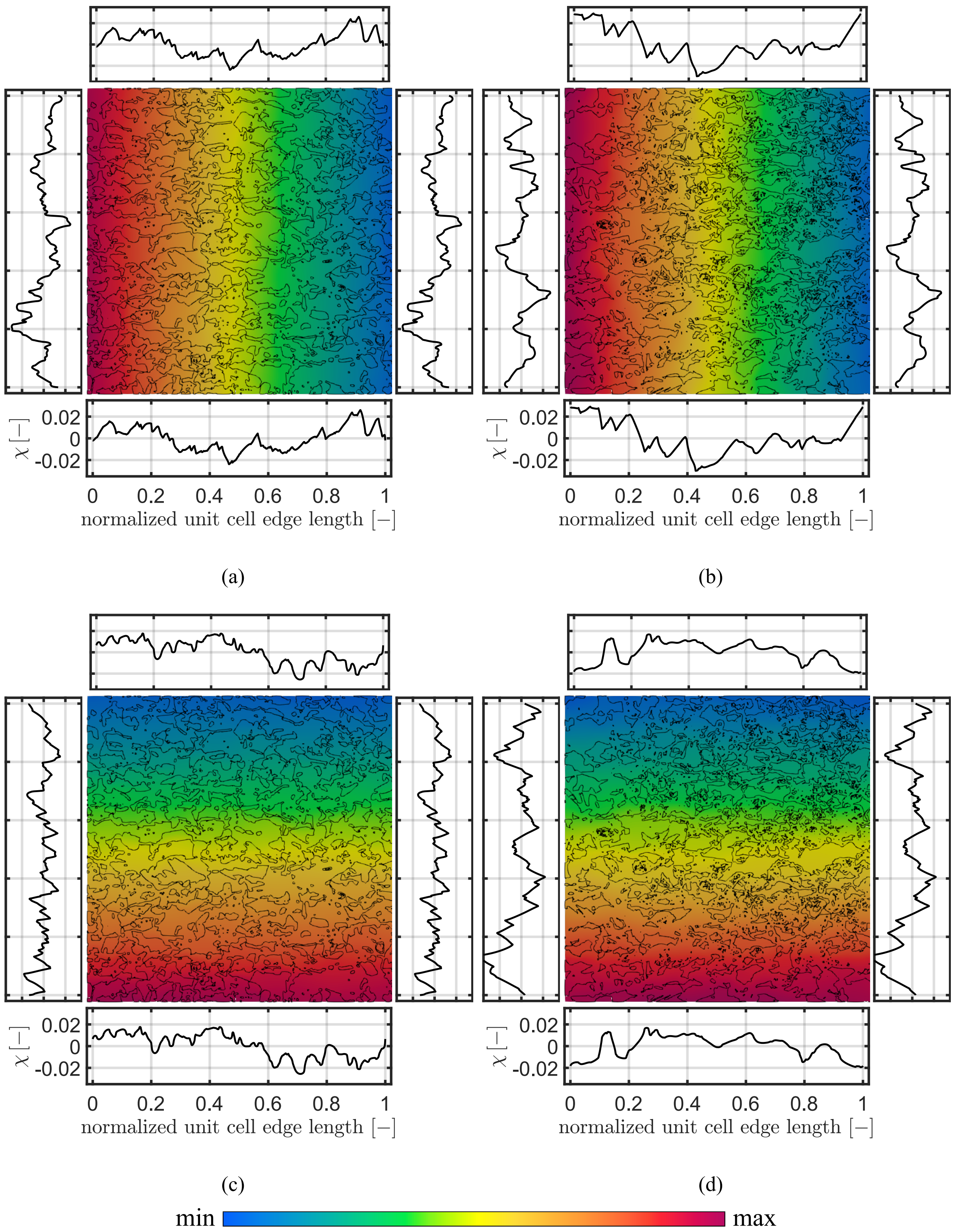

(a)

(b)

(c)

(d)

Fig. 4: Contour plots represent total magnetic scalar potential as the solution to the unit cell problem for the given unitary macroscopic field ${}^{\mathrm{M}}\boldsymbol{H} = [1, 0]^{\top}$ for (a) and (b) and ${}^{\mathrm{M}}\boldsymbol{H} = [0, 1]^{\top}$ for (c) and (d). The results are overlayed on the corresponding microstructure for which the phase boundaries are highlighted in black for DPL600-650 in (a) and (c) and for DPL600-800 in (b) and (d). The side plots show the microstructural heterogeneity mediated periodic boundary fluctuation field χ, scaled with the unit cell edge length, around the corresponding edge scalar potential average for a concise representation.

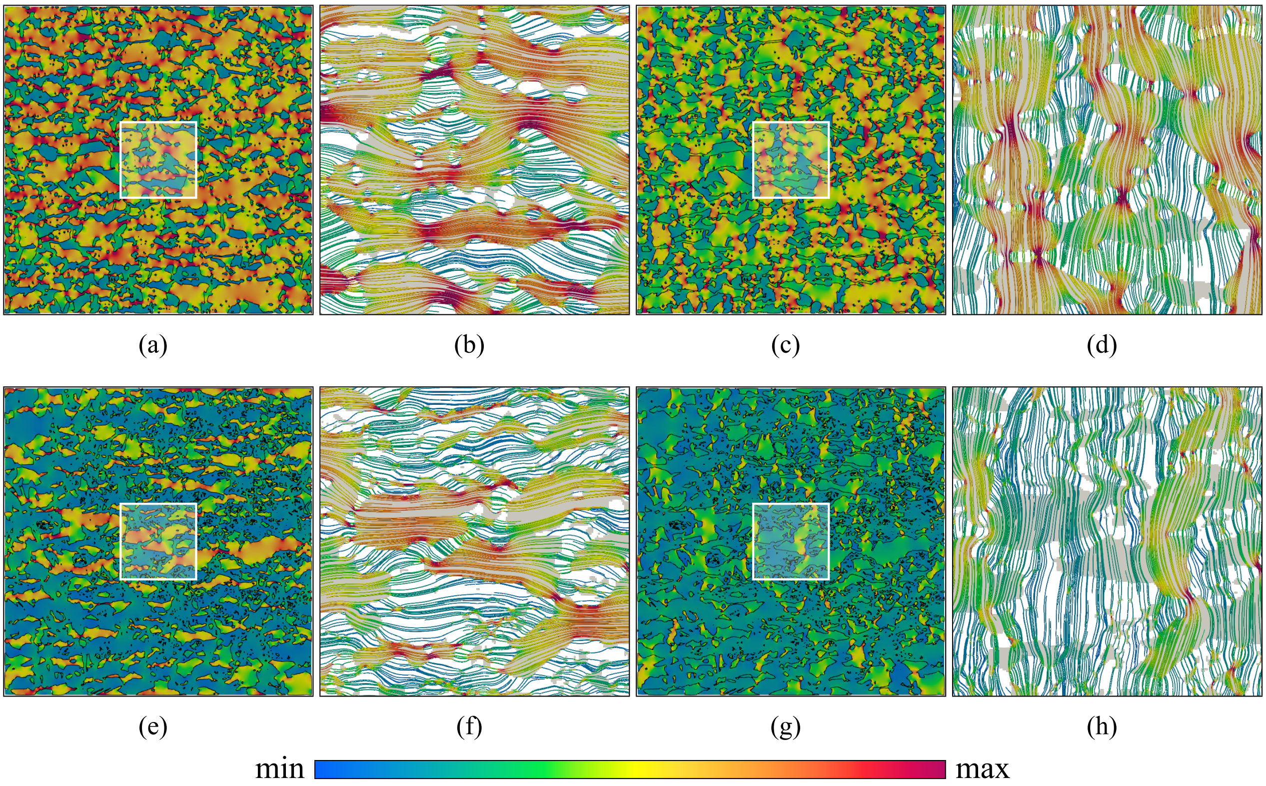

Fig. 5: The distribution of magnetic flux density as a multiple of μ_0 for the given unitary macroscopic field ${}^{\mathrm{M}}\boldsymbol{H} = [1, 0]^\top$, for (a), (b), (e), and (f), and ${}^{\mathrm{M}}\boldsymbol{H} = [0, 1]^\top$, for (c), (d), (g), and (h). The first row gives the results for the micrograph for DPL600-650 with a ferrite content of $\phi_{\mathrm{Fe}} = 0.64$ whereas, in the second row, the results are depicted for the micrograph for DPL600-800 with a ferrite content of $\phi_{\mathrm{Fe}} = 0.38$. In (a), (c), (e), and (g), the contour plots for the complete FE model is shown, whereas in (b), (d), (f), and (h), the streamlines are given for the central region marked with a white square in corresponding full images, with the background grey region denoting the ferrite phase.

The analytical predictions with mixing rules and computed magnetic permeabilities for the investigated microstructures are given in Figure 6. It is shown that our computations for the rolling direction are in agreement with those reported in [28], also only for the rolling direction. Since our methodology allows calculation of the complete effective permeability tensor, we are able to compute the effective magnitudes also for the transverse direction. Since the (symmetric) off-diagonal terms are generally two to three orders of magnitude smaller than the normal components, they are not reported here. As anticipated, increasing ferrite content increases the emerging effective magnetic permeability. In agreement with our observations regarding Fig. 5, percolating ferrite phase pathways that dominate along with the rolling direction result in anisotropy in the computed effective magnetic permeabilities, where the permeability along the rolling direction is calculated to be up to 20% higher. Coming to the mixing rule predictions, even though we do not have high contrast in constituent material properties, the Voigt and Reuss bounds are far from being stringent. Considering rolling direction, predictions with a power law with $\beta = 1/3$ and the Bruggemann mixing rule agree with the computations. Nevertheless, this agreement is lost for the effective magnetic permeability distribution in the transverse direction, which seems to be better represented by the Maxwell Garnett mixing rule. Thus, it does not seem possible to identify a universally applicable mixing rule which uses volume fraction as the mere statistical input.

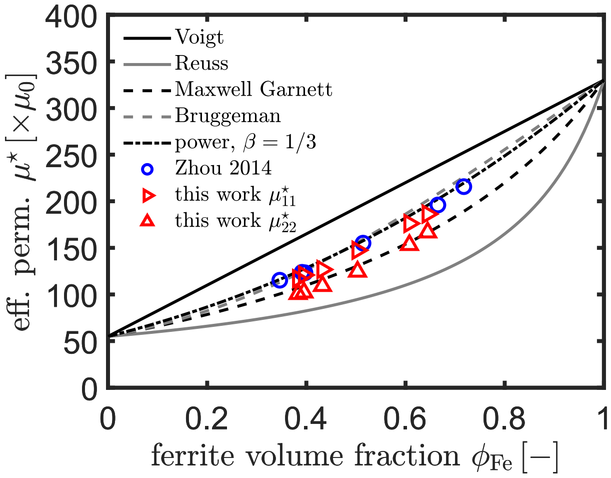

Fig. 6: Computed effective relative magnetic permeability and its comparison to various analytical solutions and the numerical solutions given in [28]. The results in [28] are provided only for the rolling direction, whereas our results are given for both the rolling and transverse directions. The mixture rules satisfy the limiting processes, such that $\mu^\star \to \mu_{\mathrm{Mar}} = 55\mu_0$ as $\phi_{\mathrm{Fe}} \to 0$ and $\mu^\star \to \mu_{\mathrm{Fe}} = 330\mu_0$ as $\phi_{\mathrm{Fe}} \to 1$.

Conclusion

The performance of various analytical rules of mixtures is compared with that of the finite element method-based first-order asymptotic homogenization in predicting the effective magnetic properties of ferritic-martensitic DP600-grade steel at the macroscale. While the considered mixture rules use only the phase volume fraction as the statistical microstructural descriptor, asymptotic homogenization with finite element method provides an accurate account of the underlying phase geometry, e.g., size, shape, topology. Thus, in contrast to the isotropic mixture rules, it allows computation of the physical properties in their complete tensorial form, permitting possible directionality. Our numerical studies for DP600 microstructures reveal magnetic permeability increasing with ferrite content with up to 20% difference between rolling and transverse directions.

Acknowledgments

This work was supported by the STW project 15472 of the STW Smart Industry 2016 program. This support is gratefully acknowledged.

References

[1] S. Vaidya, P. Ambad, and S. Bhosle. "Industry 4.0 - A Glimpse". In: *Procedia Manufacturing* 20 (2018). 2nd International Conference on Materials, Manufacturing and Design Engineering (iCMMD2017), 11-12 December 2017, MIT Aurangabad, Maharashtra, INDIA, pp. 233–238.
[2] H. Hagenah et al. "4.0 in metal forming - questions and challenges". In: *Procedia CIRP* 79 (2019). 12th CIRP Conference on Intelligent Computation in Manufacturing Engineering, 18-20 July 2018, Gulf of Naples, Italy, pp. 649–654.
[3] J. Allwood et al. "Closed-loop control of product properties in metal forming". In: *CIRP Annals* 65.2 (2016), pp. 573–596.
[4] J. Heingärtner et al. "Acquisition of material properties in production for sheet metal forming processes". In: *AIP Conference Proceedings* 1567.1 (2013), pp. 671–674.

[5] F. J. Alamos, J. C. Gu, and H. Kim. “Evaluating the Reliability of a Nondestructive Evaluation (NDE) Tool to Measure the Incoming Sheet Mechanical Properties”. In: *Forming the Future*. Ed. by G. Daehn et al. Cham: Springer International Publishing, 2021, pp. 2573–2584.

[6] P. Fischer et al. “Experiences with inline feedback control and data acquisition in deep drawing”. In: *Procedia Manufacturing* 15 (2018). Proceedings of the 17th International Conference on Metal Forming, 2018, Toyohashi, Japan, pp. 949–954.

[7] H. Yin and L. Sun. “Effective magnetic permeability of composites containing chain-structured particles”. In: *Acta Materialia* 54.9 (2006), pp. 2317–2323.

[8] W. Yin et al. “Measurement of Permeability and Ferrite/austenite Phase Fraction Using a Multifrequency Electromagnetic Sensor”. In: *2007 IEEE Instrumentation Measurement Technology Conference IMTC 2007*. 2007, pp. 1–4.

[9] W. Yin et al. “Exploring the relationship between ferrite fraction and morphology and the electromagnetic properties of steel”. In: *Journal of Materials Science* 42-16 (2017), pp. 6854–6861.

[10] L. Zhou et al. “Quantification of the phase fraction in steel using an electromagnetic sensor”. In: *NDT & E International* 67 (2014), pp. 31–35.

[11] X. Hao et al. “Modelling the electromagnetic response of two-phase steel microstructures”. In: *NDT & E International* 43.4 (2010), pp. 305–315.

[12] R. Haldane et al. “Multi-frequency electromagnetic sensor measurement of ferrite/austenite phase fraction-Experiment and theory”. In: *Scripta Materialia* 54.10 (2006), pp. 1761–1765.

[13] J. Heingärtner, M. Born, and P. Hora. “Online Acquisition of Mechanical Material Properties of Sheet Metal for the Prediction of Product Quality by Eddy Current”. In: *10th European Conference and Exhibition on Non-destructive Testing*. 2010.

[14] R. Hilzinger and W. Rodewald. *Magnetic Materials Fundamentals, Products, Properties, Applications*. Publicis Publishing, Erlangen, 2013.

[15] E. Garboczi. *Finite Element and Finite Difference Programs for Computing the Linear Electric and Elastic Properties of Digital Images of Random Materials*. en. 1998-12-01 1998.

[16] G. Chatzigeorgiou, A. Javili, and P. Steinmann. “Unified magnetomechanical homogenization framework with application to magnetorheological elastomers”. In: *Mathematics and Mechanics of Solids* 19.2 (2014), pp. 193–211.

[17] A. Javili, G. Chatzigeorgiou, and P. Steinmann. “Computational homogenization in magnetomechanics”. In: *International Journal of Solids and Structures* 50.25 (2013), pp. 4197–4216.

[18] P. Karimi et al. “Electrostatic and magnetostatic properties of random materials”. In: *Phys. Rev. E* 99 (2 Feb. 2019), p. 022120.

[19] J. C. M. Garnett and J. Larmor. “XII. Colours in metal glasses and in metallic films”. In: *Philosophical Transactions of the Royal Society of London. Series A, Containing Papers of a Mathematical or Physical Character* 203.359-371 (1904), pp. 385–420.

[20] D. A. G. Bruggeman. “Berechnung verschiedener physikalischer Konstanten von heterogenen Substanzen. I. Dielektrizitätskonstanten und Leitfähigkeiten der Mischkörper aus isotropen Substanzen”. In: *Annalen der Physik* 416.7 (1935), pp. 636–664.

[21] D. Lukkassen, L.-E. Persson, and P. Wall. “Some engineering and mathematical aspects on the homogenization method”. In: *Composites Engineering* 5.5 (1995), pp. 519–531.

[22] B. Eidel and A. Fischer. “The heterogeneous multiscale finite element method for the homogenization of linear elastic solids and a comparison with the FE2 method”. In: *Computer Methods in Applied Mechanics and Engineering* 329 (2018), pp. 332–368.

[23] J. Fish. *Practical Multiscaling*. John Wiley and Sons, Chichester, 2014.

[24] C. Soyarslan, M. Pradas, and S. Bargmann. “Effective elastic properties of 3D stochastic bicontinuous composites”. In: *Mechanics of Materials* 137 (2019), p. 103098.

[25] L. H. Ma, Q. S. Rolfe B. F.and Yang, and C. H. Yang. “A New Solution Method for Homogenization of Effective Properties of Electromagnetic Honeycombs”. In: *Key Engineering Materials* 443 (2010), pp. 551–556.

[26] J. C. Maxwell. *A Treatise on Electricity and Magnetism*. Oxford University Press, 1783.

[27] SIMULIA. *ABAQUS/Standard User’s Manual, Version 2019*. English. United States: Dassault Systèmes Simulia Corp, 2009.

[28] L. Zhou. “Non-destructive Characterisation of Steel Microstructures Using Electromagnetic Sensors”. PhD thesis. University of Birmingham, 2014.

[29] J. Schindelin et al. “Fiji: an open-source platform for biological-image analysis”. In: *Nature Methods* 9 (7 2012), pp. 676–682.

[30] T. W. Ridler and S. Calvard. “Picture Thresholding Using an Iterative Selection Method”. In: *IEEE Transactions on Systems, Man, and Cybernetics* 8.8 (1978), pp. 630–632.